# Electronic Supplementary Information

## Direct $CO_2$ photoreduction from flue gas by synergistic catalysis of a nickel metal-organic framework and a ruthenium polypyridyl complex

Man Dong,[†a] Yu Tian,[†c] Jian-Xia Gu,[a,d] Xiao-Hui Wang,[a] Lin-Xin Wang,[a] Bao-Shan Hou,[a] Afifa Yousuf,[a] Chun-Yi Sun,*[a] Jie Wu,[e] Zhen-Hui Kang,*[e] Xin-Long Wang,*[a] and Zhong-Min Su[b]

[a]Key Laboratory of National & Local United Engineering Laboratory for Power Battery Institution, Northeast Normal University, Changchun, Jilin, 130024, P. R. China. E-mail: suncy009@nenu.edu.cn; wangxl824@nenu.edu.cn

[b]State Key Laboratory of Supramolecular Structure and Materials, Institute of Theoretical Chemistry, College of Chemistry, Jilin University, Changchun 130021, China.

[c]Institute for Interdisciplinary Quantum Information Technology, Jilin Engineering Normal University, Changchun, 130052, P. R. China.

[d]Department of Chemistry, Xinzhou Teachers University, Xinzhou, 034000, P. R. China.

[e]Jiangsu Key Laboratory for Carbon-Based Functional Materials & Devices, Institute of Functional Nano & Soft Materials (FUNSOM), Soochow University, Suzhou, Jiangsu, 215123, P. R. China. E-mail: zhkang@suda.edu.cn

*Corresponding author: e-mail: suncy009@nenu.edu.cn; zhkang@suda.edu.cn；wangxl824@nenu.edu.cn

## Experimental Section

### Materials characterizations

All the reagents and solvents were purchased from commercial sources and used without further purification.

Crystallographic data of Ni-MOF1 was collected on a Bruker Apex-II CCD. Powder X-ray diffractions (PXRD) patterns were recorded on a Siemens D5005diffractometer with Cu KR (λ =1.5418 Å) radiation in the range of 5-50°. The FT-IR spectra were recorded from KBr pellets in the range 4000-500 $cm^{-1}$ on a MattsonAlpha-Centauri spectrometer. UV-Vis absorption spectra were obtained by using a Shimadzu UV-2550 spectrophotometer in the wavelength range of 200-800 nm. TGA was performed on a Perkin-Elmer TG-7 analyzer heated from roomtemperature to 800ºC at a ramp rate of 10 °C $min^{-1}$ under nitrogen. The number of incident photons was tested employing a MC-LED-M Xe lamp. The gas product inphotocatalytic reactionwas measured by Shimadzu Gas Chromatography. All of the DFT calculations were performed by using Vienna ab initio simulation pachage (VASP). The transient photovoltage (TPV) responses were carried out by a homemade measurement system. The samples were excited with a laser radiation pulse (wavelength of 355 nm and pulse width of 5 ns) from a third harmonic Nd: YAG laser (Polaris II, New Wave Research, Inc.). The TPV signal was registered by a 5-GHz digital phosphor oscilloscope (MDO3104, Tektronix). Transient absorption (TA) was performed on a femtosecond transient absorption setup using a mode-locked Ti: sapphire laser/amplifier system (Solstice, Spectra-Physics).

### Calculation method of selectivity for CO

The selectivity for CO was calculated using the equation below, in which R ($mmolg^{-1}$) refers to the yield of the product under 10% $CO_2$ concentration within a certain period using irradiating with a PLS-SXE300 Xe lamp with a 420 nm.

$$Selectivity \text{ for CO} = \frac{\text{R (CO)}}{\text{R (H}_2\text{)} + \text{R (CO)}} \times 100\%$$

**Quantum yield measurement**

The apparent quantum yield (A.Q.Y.) was tested under the reaction condition of 10% $CO_2$ concentration, which was irradiated by a MC-LED-M Xe lamp with a monochromatic light beam. The A.Q.Y. was calculated according to the equation below:

$$A.Q.Y.(CO)\% = \frac{2 \times \text{number of evolved (CO) molecules}}{\text{number of incident electrons}} \times 100\%$$

The the number of incident photons was calculated as follow:

$$N = \frac{\mathrm{I} \times \mathrm{S} \times \mathrm{t} \times \lambda}{\hbar \times \mathrm{c}}$$

Where, ħ is the Planck constant ($6.626 \times 10^{-34}$ J s), c is the speed of light ($3 \times 10^{8}$ m $s^{-1}$), S is the irradiation area (φ=0.5 cm), I is the intensity of irradiation light (136 mW $cm^{-2}$), t is the photoreaction time (1800 s), λ is the incident wavelength (420 nm).

**Texting of transient photovoltage (TPV)**

The TPV self-made device consists of three parts: ITO coated with sample as working electrode, Pt wire as counter electrode and signal collector in the middle. For data acquisition and processing, the signal collector is transmitted to the computer, and the modeling software is used to perform data output.

The transient photovoltage measurements were conducted under room temperature on films with area of samples (1 cm × 1 cm) deposited on indium-tin oxide(ITO) glass substrates. The films of the samples were prepared by drop-coating 5 mg $mL^{-1}$ aqueous (700 $\mu$L water, 250 $\mu$L ethanol and 50 $\mu$L of Nafion solution) dispersions of the samples on ITO slides, then dried in air. The ITO glass modified with samples as the working electrodes and Pt wire as the counter electrodeswere wetted with $CO_2$ saturated acetonitrile/$H_2O$ aqueous (v/v = 4:1) or (adding $N_2$ saturated acetonitrile/$H_2O$). At room temperature, the transient photovoltage (TPV) responses were performed on a self-made system. The samples were excited a laser radiation pulse

(wavelength 355 nm, pulse width 5 ns) from a third-harmonic Nd: YAG laser (Polaris II, New Wave Research, Inc.). The TPV signal was amplified and recorded by a 5 GHz digital phosphorylation oscilloscope (MDO3104, Tektronix). The photocurrent is obtained by the ratio of the photovoltage to the system impedance.

The TPV technology is an effective means to study the dynamics of the photogenerated charge transport process. Current intensity represents the concentration of photogenerated charge generated by the material. The maximum charge extraction efficiency, i.e., the total amount of charge extracted, is expressed by the integrated area. In addition, the photogenerated charge recombination rate is evaluated by time attenuation constants (τ) of photogenerated charge.

**Computational methods and models**

All of the DFT calculations were performed by using Vienna ab initio simulation package (VASP).[1-2] The exchange-correlation energy is treated based on the generalized gradient approximation (GGA) in the scheme of Perdew-Burke-Ernzerhof (PBE).[3] The core-electron interactions are described by Projector-augmented-wave (PAW) pseudopotentials.[4] To describe the van der Waals (vdW) interaction in the systems properly, DFT with the empirical dispersion correction (DFT-D3) method is applied due to its good description of long-range vdW interactions.[5] The Ni-MOF1 (100) surfaces observed in the experiment were modeled with $[Ru(bpy)_3]Cl_2$. The vacuum space in the z direction was set to 15 Å to avoid the unwanted interaction between the slab and its period images. During the geometry optimization, half of the atoms of Ni-MOF1 (100) on the bottom layers were fixed in their bulk positions. A 2 × 2 × 1 Monkhorst-Pack k-point grid was adopted for calculations on Ni-MOF1 and $[Ru(bpy)_3]Cl_2$/Ni-MOF1. The k-point were sampled using a 2 × 2 × 2 Monkhorst-Pack mesh for $[Ru(bpy)_3]Cl_2$ calculation. The energy cutoff is set to be 420 eV. All atoms were fully relaxed until the total energy converges to less than $10^{-4}$ eV and the ionic relaxation were performed until the force on each atom converge to within 0.03 eV $Å^{-1}$.

The free-energy change ($\Delta G$) of each elementary reaction step on these electrocatalysts was calculated according to the computational hydrogen electrode (CHE) model suggested by Nørskov et al.[6-8] According to this method, the reaction free energies of the NRR steps were calculated as: $\Delta G = \Delta E + \Delta E_{ZPE} - T\Delta S$, where $\Delta E$ is the electronic energy difference directly obtained from DFT calculations, $\Delta E_{ZPE}$ is the change in zero-point energies, T is the temperature (T = 298.15 K), and $\Delta S$ is the entropy change. The entropies and vibrational frequencies of molecules in the gas phase were taken from the NIST database, while the vibrational frequencies of adsorbed species were computed to obtain ZPE contribution in the free energy expression.[9-11] Only adsorbate vibrational modes were computed explicitly, while the catalyst sheet was fixed (assuming that vibrations of the substrate are negligible).

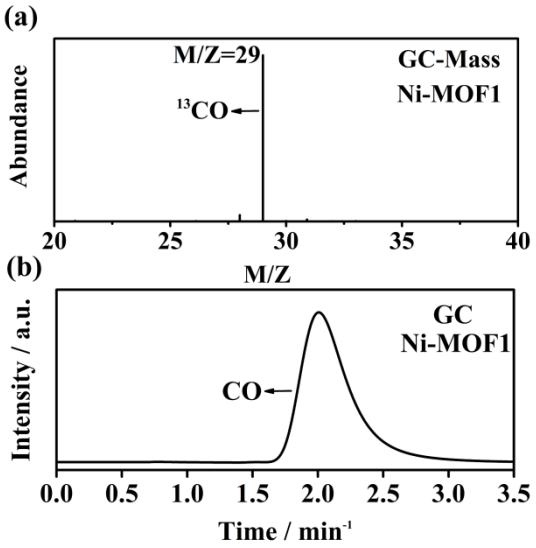


**Fig. S1** GC-Mass result under $^{13}CO_2$ atmosphere (a) and the corresponding GC spectrum of (b).

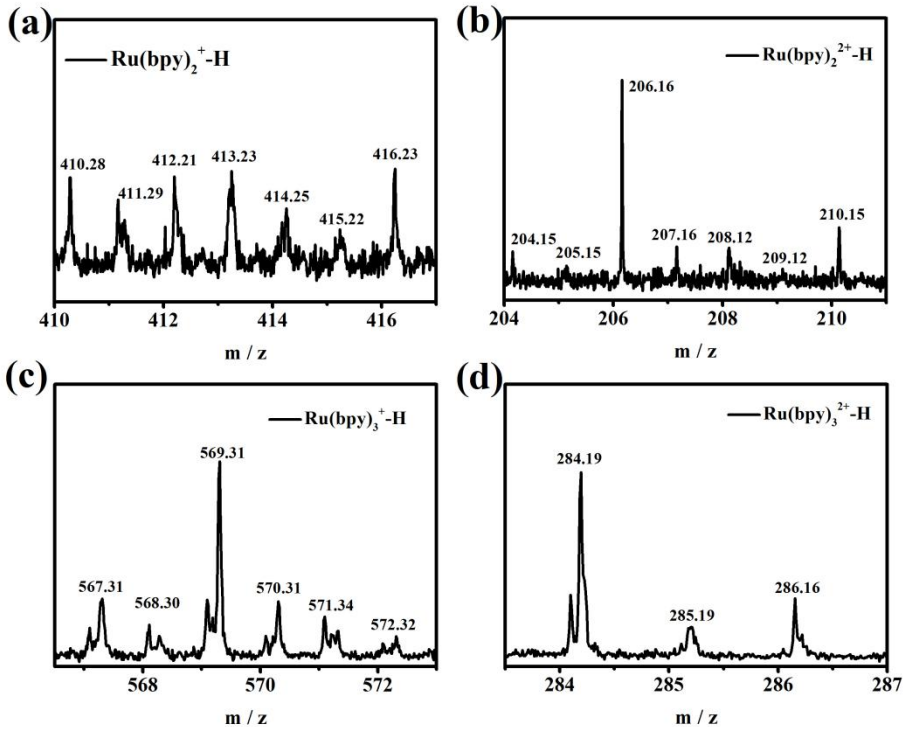


**Fig. S2** The MS analysis of the system after photocatalytic reaction (a) $Ru(bpy)_2^{+}$-H; (b) $Ru(bpy)_2^{2+}$-H; (c) $Ru(bpy)_3^{2+}$-H; (d) $Ru(bpy)_3^{+}$-H.

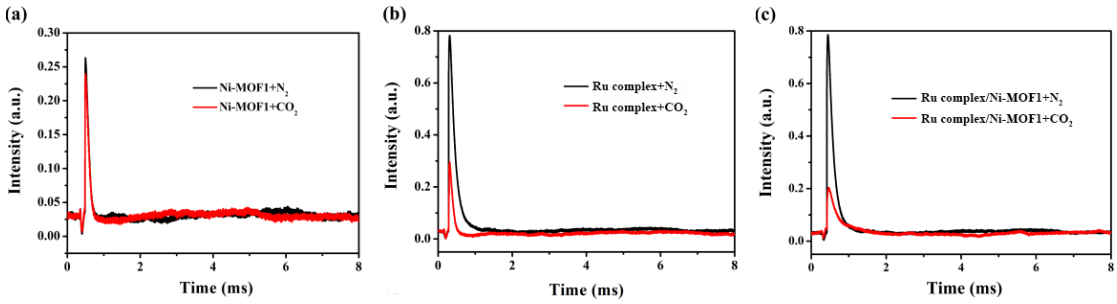


**Fig. S3** (a), (b) and (c) Comparison of the *In situ* TPV with bare Ru complex, Ni-MOF1 or the composite electrodes after adding $N_2$ or $CO_2$.

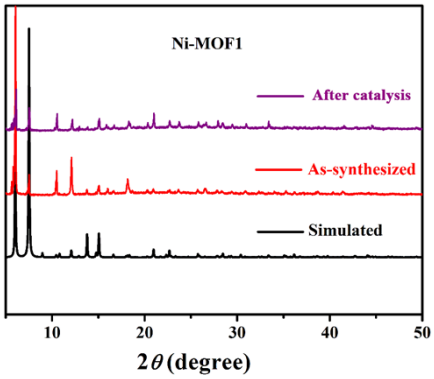


**Fig. S4** Powder X-ray diffraction (PXRD) of Ni-MOF1 (black curve: simulated structure, red curve: as-synthesized sample, purple curve: the sample after $CO_2$ photoreduction).

**Table S1.** The Crystallographic data for Ni-MOF1.

| Compound | Ni-MOF1 |
|---|---|
| Chemical formula | $C_{30}H_{24}O_{16}S_6Ni_3$ |
| Formula weigh | 1009.02 |
| Crystal system | Hexagonal |
| Space group | *P6₃/mmc* |
| *a* (Å) | 16.907 |
| *b* (Å) | 16.907 |
| *c* (Å) | 19.713 |
| *α* (°) | 90 |
| *β* (°) | 90 |
| *γ*(°) | 120 |
| **V** (Å$^3$) | 4880 |
| *Z* | 2 |
| $D_{calcd}$[g cm$^{-3}$] | 0.687 |
| *F*(000) | 1024 |
| GOF on $F^2$ | 1.071 |
| $R_1$ [ $I > 2\sigma(I)$]$^a$ | 0.0646 |
| w$R_2$$^b$ (all data) | 0.2213 |
| $R_{int}$ | 0.150 |

$^aR_1 = \Sigma\,||F_o|-|F_c||\,/\Sigma\,|F_o|$. $^bwR_2 = |\Sigma w(|F_o|^2-|F_c|^2)|/\Sigma\,|w\,(F_o^2)^2|^{1/2}$.

**Table S2.** Photoreduction of pure and diluted $CO_2$ systems.

| Catalyst | Concentration of $CO_2$ | Yield of CO (mmol $g^{-1}$) | $CO_2$reduction selectivity | *A.Q.Y.%* | Photosensitizer Sacrificial agent | *Ref.* |
|---|---|---|---|---|---|---|
| $NiCo_2O_4$ | 100% | 10.5 | 93.4% | 1.86 | $Ru(bpy)_3^{2+}$ | S[12] |
| | 10% | 8.9 | 89% | 1.56 | TEOA | |
| Ni MOLs | 100% | 25 | 97.8% | 2.2 | $Ru(bpy)_3^{2+}$ | S[13] |
| | 10% | 25 | 96.8% | 1.96 | TEOA | |
| Ni-TpBpy | 100% | 4.06 | 96% | 0.3 | $Ru(bpy)_3^{2+}$ | S[14] |
| | 10% | 0.92 | 76% | — | TEOA | |
| MAF-X27l-Cl | 100% | 6.35 | 98.2% | 2.0 | $Ru(bpy)_3^{2+}$ | S[15] |
| | 10% | 5.20 | 97.8% | — | TEOA | |
| r-NiO | 100% | 4.37 μmol·$h^{-1}$ | 90.47% | / | $Ru(bpy)_3^{2+}$ | S[16] |
| | 10% | 3.14 μmol·$h^{-1}$ | 70% | 0.46 | TEOA | |
| COF-367-Co NS | 100% | 10.16 mmol·$g^{-1}$·$h^{-1}$ | 78% | / | $Ru(bpy)_3^{2+}$ | S[17] |
| | 10% | 2.587 mmol·$g^{-1}$·$h^{-1}$ | 72% | / | ascorbic acid | |
| Ni-TpBpy | 100% | 4.057 | 96% | / | $Ru(bpy)_3^{2+}$ | S[18] |
| | 10% | 0.915 | 76% | / | TEOA | |
| Ru(II)-Re(I) dinuclear complex | 100% | 0.017 $s^{-1}$ | 100% | 0.5 | TEOA | S[19] |
| | 10% | 0.017 $s^{-1}$ | 100% | 0.5 | BIH | |
| Ni-COFs | 100% | 10.62 μmol $h^{-1}$ | 94.8% | / | $Ru(bpy)_3^{2+}$ | S[20] |
| | 10% | 9.06 μmol $h^{-1}$ | 88.6% | / | TEOA | |
| Ni@TPHH-COF | 100% | 1.27 mmol·$g^{-1}$·$h^{-1}$ | 99.2% | / | $Ru(bpy)_3^{2+}$ | S[21] |
| | 10% | 3.28 mmol·$g^{-1}$·$h^{-1}$ | 95% | 3.96 | TEOA | |
| $[Ru(bpy)_3]/[Co_{20}Mo_{16}P_{24}]$ | 100% | 74.9 mmol·$g^{-1}$·$h^{-1}$ | / | 1.5% | $Ru(bpy)_3^{2+}$ | S[22] |
| | 10% | 44.9 mmol·$g^{-1}$·$h^{-1}$ | / | / | TEOA | |
| V-$Ni(OH)_2$ NSs | 100% | 20.7 μmol | 97.2% | 1.28 | $Ru(bpy)_3^{2+}$ | S[23] |
| | 10% | 5.8 μmol $h^{-1}$ | 91.3% | / | TEOA | |
| Ni-MOF1 | 100% | 9.37 | 98.3% | — | $Ru(bpy)_3^{2+}$ | This work |
| | 10% | 23.13 | 84.3% | **2.1** | TEOA | |

## References

(S1) Kresse G.; Furthmuller J. Efficient iterative schemes for ab initio total-energy calculations using a plane-wave basis set. *Phys. Rev. B: Condens. Matter Mater. Phys.* **1996,** *54* (16), 11169.

(S2) Kresse G.; Furthmuller J. Efficiency of ab-initio total energy calculations for metals and semiconductors using a plane-wave basis set. *Comput. Mater. Sci.* **1996,** *6* (1), 15-50.

(S3) Perdew J. P.; Burke K.; Ernzerhof M. Generalized Gradient Approximation Made Simple. *Phys. Rev. Lett.* **1996,** *77* (18), 3865.

(S4) Blochl, P. E. Projector Augmented-Wave Method. *Phys. Rev. B: Condens Matter* **1994,** *50* (24), 17953-17979.

(S5) Van Troeye, B.; Torrent, M.; Gonze, X. Interatomic Force Constants Including the Dft-D Dispersion Contribution. *Phys. Rev. B* **2016,** *93*, 3865.

(S6) Nørskov J. K.; Rossmeisl J.; Logadottir A.; Lindqvist L.; Kitchin J. R.; Bligaard T.; Jónsson H. Origin of the Overpotential for Oxygen Reduction at a Fuel-Cell Cathode. *J. Phys. Chem. B* **2004,** *108* (46), 17886.

(S7) Rossmeisl, J.; Logadottir, A.; Nørskov, J. K. Electrolysis of Water on (Oxidized) Metal Surfaces. *Chem. Phys.* **2005,** *319* (1), 178-184.

(S8) Peterson A. A.; Abild-Pedersen F.; Studt F.; Rossmeisl J.; Nørskov J. K. How copper catalyzes the electroreduction of carbon dioxide into hydrocarbon fuels. *Energy Environ. Sci.* **2010,** *3* (9), 1311.

(S9) Lim, D.-H.; Wilcox, J. Mechanisms of the Oxygen Reduction Reaction on Defective Graphene-Supported Pt Nanoparticles from First-Principles. *J. Phys. Chem. C* **2012,** *116* (5), 3653-3660.

(S10) Wang, Y.; Yuan, H.; Li, Y.; Chen, Z. Two-Dimensional Iron-Phthalocyanine (Fe-Pc) Monolayer as a Promising Single-Atom-Catalyst for Oxygen Reduction Reaction: A Computational Study. *Nanoscale* **2015,** *7* (27), 11633-11641.

(S11) Kattel, S.; Atanassov, P.; Kiefer, B. Density Functional Theory Study of Ni–Nx/C Electrocatalyst for Oxygen Reduction in Alkaline and Acidic Media. *J. Phys. Chem. C* **2012,** *116* (33), 17378-17383.

(S12) Han, B.; Song, J.; Liang, S.; Chen, W.; Deng, H.; Ou, X.; Xu, Y.-J.; Lin, Z. Hierarchical $NiCo_2O_4$ Hollow Nanocages for Photoreduction of Diluted $CO_2$: Adsorption and Active Sites Engineering. *Appl. Catal. B Environ.* **2020,** *260*, 118208.

(S13) Han, B.; Ou, X.; Deng, Z.; Song, Y.; Tian, C.; Deng, H.; Xu, Y. J.; Lin, Z. Nickel Metal-Organic Framework Monolayers for Photoreduction of Diluted $CO_2$: Metal-Node-Dependent Activity and Selectivity. *Angew. Chem. Int. Ed.* **2018,** *57* (51), 16811-16815.

(S14) Zhong, W.; Sa, R.; Li, L.; He, Y.; Li, L.; Bi, J.; Zhuang, Z.; Yu, Y.; Zou, Z. A Covalent Organic Framework Bearing Single Ni Sites as a Synergistic Photocatalyst for Selective Photoreduction of $CO_2$ to CO. *J. Am. Chem. Soc.* **2019,** *141* (18), 7615-7621.

(S15) Wang, Y.; Huang, N. Y.; Shen, J. Q.; Liao, P. Q.; Chen, X. M.; Zhang, J. P. Hydroxide Ligands Cooperate with Catalytic Centers in Metal-Organic Frameworks for Efficient Photocatalytic $CO_2$ Reduction. *J. Am. Chem. Soc.* **2018,** *140* (1), 38-41.

(S16) Chen, W.; Liu, X.; Han, B.; Liang, S.; Deng, H.; Lin, Z., Boosted photoreduction of diluted $CO_2$ through oxygen vacancy engineering in NiO nanoplatelets. *Nano Res.* **2020,** *14*, 730-737.

(S17) Liu, W.; Li, X.; Wang, C.; Pan, H.; Liu, W.; Wang, K.; Zeng, Q.; Wang, R.; Jiang, J., A Scalable General Synthetic Approach toward Ultrathin Imine-Linked Two-Dimensional Covalent Organic Framework Nanosheets for Photocatalytic $CO_2$ Reduction. *J. Am. Chem. Soc.* **2019,** *141* (43), 17431-17440.

(S18) Zhong, W.; Sa, R.; Li, L.; He, Y.; Li, L.; Bi, J.; Zhuang, Z.; Yu, Y.; Zou, Z., A Covalent Organic Framework Bearing Single Ni Sites as a Synergistic Photocatalyst for Selective Photoreduction of $CO_2$ to CO. *J. Am. Chem. Soc.* **2019,** *141* (18), 7615-7621.

(S19) Nakajima, T.; Tamaki, Y.; Ueno, K.; Kato, E.; Nishikawa, T.; Ohkubo, K.; Yamazaki, Y.; Morimoto, T.; Ishitani, O., Photocatalytic Reduction of Low Concentration of $CO_2$. *J. Am. Chem. Soc.* **2016,** *138* (42), 13818-13821.

(S20) Han, B.; Ou, X.; Zhong, Z.; Liang, S.; Deng, H.; Lin, Z., Rational Design of FeNi Bimetal Modified Covalent Organic Frameworks for Photoconversion of Anthropogenic $CO_2$ into Widely Tunable Syngas. *Small* **2020,** *16* (38), 2002985-2002991.

(S21) Dong, M.; Zhou, J.; Zhong, J.; Li, H.-T.; Sun, C.-Y.; Han, Y.-D.; Kou, J.-N.; Kang, Z.-H.; Wang, X.-L.; Su, Z.-M. $CO_2$ Dominated Bifunctional Catalytic Sites for Efficient Industrial Exhaust Conversion. *Adv. Funct. Mater.* **2021**, 2110136.

(S22) Xu, H.; You, S.; Lang, Z.; Sun, Y.; Sun, C.; Zhou, J.; Wang, X.; Kang, Z.; Su, Z., Highly Efficient Photoreduction of Low-Concentration $CO_2$ to Syngas by Using a Polyoxometalates/$Ru^{II}$ Composite. *Chem-Eur J* **2020,** *26* (12), 2735-2740.

(S23) Liang, S.; Han, B.; Ou, X.; Ye, X.; Chen, W.; Deng, H.; Tian, C.; Lin, Z., Lattice-strained nickel hydroxide nanosheets for the boosted diluted $CO_2$ photoreduction. *Environ. Sci-Nano* **2021,** *8*, 2360-2371.